Microscopy Research and Technique

WILEY

MICROSCOPY RESEARCH & TECHNIQUE

PRIMERS IN MICROSCOPY OPEN ACCESS

MINFLUX Nanoscopy: A "Brilliant" Technique Promising Major Breakthrough

Marco Salerno[1] | Virginia Bazzurro[1] | Elena Angeli[1] | Paolo Bianchini[2] | Mohammadmehdi Roushenas[1] | Kimiya Pakravanan[1] | Alberto Diaspro[1,2]

[1]Dipartimento di Fisica, Università di Genova, Genova, Italy | [2]Nanoscopy and NIC@IIT, CHT, Istituto Italiano di Tecnologia, Genova, Italy

Correspondence: Marco Salerno (marco.salerno@unige.it) | Alberto Diaspro (alberto.diaspro@iit.it)

Received: 20 September 2024 | **Revised:** 13 November 2024 | **Accepted:** 24 November 2024

Review Editor: Paul Verkade

Funding: This work was supported by SEELIFE ("StrEngthEning the ItaLian InFrastructure of Euro-bioimaging") that was funded by the European Union - Next Generation EU PNRR MUR Infrastructure program (B53C22001810006, IR0000023).

Keywords: fluorescent labels | single-molecule localization | single-molecule tracking | super-resolution microscopy

ABSTRACT

MINFLUX nanoscopy relies on the localization of single fluorophores with expected ~2 nm precision in 3D mapping, roughly one order of magnitude better than standard stimulated emission depletion microscopy or stochastic optical reconstruction microscopy. This "brilliant" technique takes advantage of specialized localization principles and algorithms that require only dim fluorescence signals with a minimum flux of photons; hence the name follows. With this level of performance, MINFLUX imaging and tracking should allow for the routine study of biological processes down to the molecular scale, revealing previously unresolved details in cell structures, such as the organization of calcium channels in muscle cells or the clustering of receptors in synapses. Whereas the high localization precision is definitely a strength of the MINFLUX technique, limitations and challenges also exist, especially in the labeling procedures aiming at appropriate density and on/off switching kinetics. This primer presents some significant results achieved with MINFLUX so far and highlights specific operational procedures crucial for this technique.

1 | Introduction: From Resolution to Precise Localization

The importance of high resolution and sensitivity in optical microscopy, especially aiming at advances in life sciences applications, is well known and recognized (Diaspro 2010; Diaspro & van Zandvoort, 2021). In the past two decades, most progress has been initially carried out by stimulated emission depletion microscopy (STED) (Vicidomini, Bianchini, Diaspro 2018; Cella Zanacchi et al. 2011; Galiani et al. 2012; Bianchini et al. 2015). More recently, localization techniques have promised to reach unprecedented results in this field (Scalisi, Pisignano, and Cella Zanacchi 2023). As compared to the standard localization approach, where precision σ scales as $1/\sqrt{N}$, with N being the number of required photons, which is linked to the Abbe resolution limit formula (Diaspro and Bianchini 2020), the MINFLUX approach to localization minimizes N. This removes issues of either background (i.e., low signal-to-noise) or photobleaching (extreme exploitation of photon budget from the fluorophores) by actually retrieving information from not-emitted light (Balzarotti et al. 2017). A smart scan is performed during MINFLUX measurements by combining a rough confocal Gaussian beam mapping with switching to excitation by a donut beam. This beam is shaped similarly to that used in STED (Hell and Wichmann 1994; Lukinavičius et al. 2024) for engineering the point spread function, yet is used for excitation and is the key to obtain high-precision localization of the fluorophore with few

Summary

- MINFLUX is a recent single-molecule localization microscopy technique.
- The technique allows nanoscale resolution imaging and fast tracking.
- A number of biological problems can be addressed with this technique.

photons (see Figure 1a). The most accurate fluorophore position is given by probing along pre-defined spots in a circle (see colored dots in Figure 1b) and interpolating signal intensities (Xiao and Ha, 2017) to find the position ideally providing the least amount of photons. Precision is then recursively improved by using a smaller and smaller circle (diameter L), moving it across several positions close to the estimated molecule position. As a result, the typical improvement in imaging quality when compared with former localization techniques is shown in Figure 1c. For 3D, instead of a simple planar set of positions distributed along the circle as in Figure 1b, more positions also offset above and below the xy plane are considered. An optimized pattern is made by 7 positions arranged in an octahedron, which sometimes involves compromising in localization precision (typically ~3 nm). The MINFLUX approach gives better precision than a camera (Gwosch et al. 2020), still a long acquisition time is required (~ 30 min) for the localization image build-up to occur, emerging from accumulation of the dense fluorophores emitting in the field of view at separate time instants (Balzarotti et al. 2017; Gwosch et al. 2020).

2 | Standard Imaging Test Sample: Nuclear Pore Complexes

A typical structure used as a standard benchmark for MINFLUX super-resolution demonstration is the protein complex of cell nuclear membrane pores (nuclear pore complex [NPC]). NPCs have been imaged with localization techniques even before the advent of MINFLUX (Owen, Sauer, and Gaus 2012) and are also routinely used as a calibration structure for example, expansion microscopy. However, they have become a kind of reference sample only with nm-scale resolution being reached more easily over the years and almost routinely today (Thevathasan et al. 2019). Here, the nucleoporins NuP107 from cell line HepG2, as imaged by 2D MINFLUX in our lab, are shown (Figure 2d, Flux640 labeling). Sample preparation was done as described later in Appendix A.

It should be mentioned that we aim for the highest possible labeling density of the structure without over-labeling, in order to have the required density of fluorescent labels emitting at a single time instant: sparse enough to allow their individual localization, yet not so few to prevent fine image reconstruction. To this goal, given, for example, a blinking buffer strategy, a balance between active and inactive fluorophores has to be gained at the region of interest before starting the MINFLUX process. This is obtained by pushing the fluorophores into a triplet state of the excited electrons (which is "dark" for fluorescence due to the improbable transition down to ground singlet state, involving the electron spin flip) with the confocal laser and (re-)activating them with a UV laser, respectively, until a reasonable count of events is seen in the software. For example, to obtain

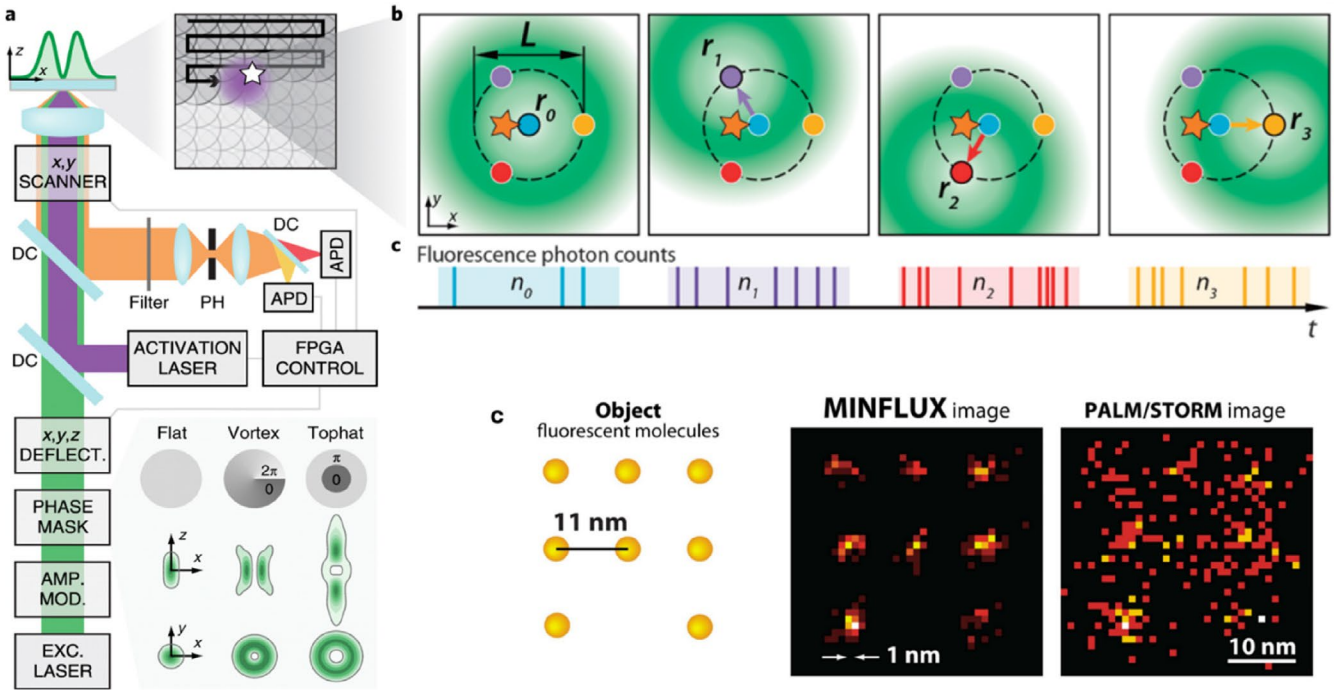

FIGURE 1 | (a) combined scanning with Gaussian beams (UV for fluorophores activation, in violet, and orange for excitation) in raster scheme, for confocal identification of emitting fluorophores, and subsequent zooming-in and re-centering with donut beam (green), for precise localization (reproduced with permission from (Gwosch et al. 2020)). (b) MINFLUX procedure for increasingly precise localization: The colored spot positions are tested for the donut center, and the best (closest to the fluorophore—star) is that one giving the least number of fluorescence photons (cyan in this case), (reproduced with permission from (Balzarotti et al. 2017)). (c) example of localization maps obtained by Minflux as compared to traditional localization approaches (PALM and STORM), (reproduced with permission from (Gwosch n.d.).

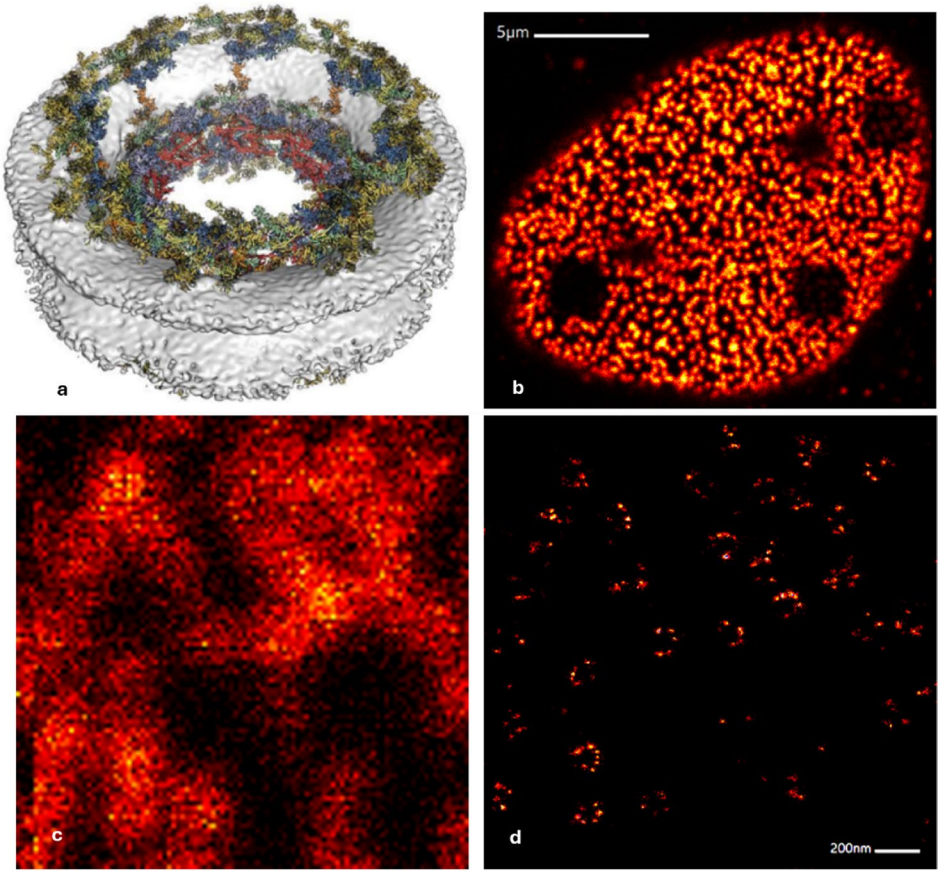

FIGURE 2 | (a) Biochemical model of a human NPC (reproduced with permission from (Petrovic et al. 2022)). (b) dark squares inside a cell nucleus point out the regions of interest where fluorophores were brought into the dark state by pre-scanning with the confocal laser before starting the MINFLUX localization process. (c) confocal image (before starting the MINFLUX process) and (d) MINFLUX 2D image (rendered xy map of localizations) obtained in the same region. Some details of the imaging method for this sample are reported in Appendix A.

our image of Figure 3d, in a typical 2D fictitious map of signals showing bursts over time, for a scan size of 2 μm corresponding to 100 pixels each with a dwell-time of, 5 μs, before starting the actual MINFLUX acquisition, strikes should appear with a fluctuating frequency in the order of few Hz. Usually, turning the fluorophores dark is the most required action rather than (re-)activation, as confirmed by the dark regions shown in Figure 2b (see legend for details). It should be stressed that this switching off the fluorophores is not photobleaching but just a temporary transition to a long-lived yet reversible dark state.

The MINFLUX image in Figure 2d points out the eight nucleoporin sub-units of one of the two rings (see the biochemical model in Figure 2a). On the contrary, in the confocal image obtained previously in the same region (Figure 2c), one can hardly identify the single pores as blobs. After the MINFLUX mapping, the scanned regions appear to have been turned off (dark state) by the confocal scan occurring before the MINFLUX process (Figure 2b).

In Figure 2d, the valid localization positions are rendered, with the color scale intensity (the brighter the higher), representing just the number of repeated localizations in the same pixel position. Alternative renderings can be set, representing different parameters that quantify the image quality. The most important is probably the center frequency ratio (cfr), that is, the ratio of emission frequency in the center of the excitation pattern over the mean emission frequency across all outer positions. Normally, single fluorophore emission events occur in the system at a frequency peak around 40 kHz, whereas a second broad peak occurs at ~80 kHz for double emission from the same fluorophore. In this case, "cfr" (comprised between 0 and 1) is better being higher, for example, 0.8 versus 0.5 (Salerno and Bazzurro n.d.). Another useful parameter is "tim" (Abberior n.d.), namely the time (in seconds) of localization during the accumulated scans: when no more localizations with recent time (bright color) appear, it means that most of what could be extracted from the given sample area in current conditions was done, and image collection can be stopped.

As previously mentioned, NPCs can be imaged also in 3D (Gwosch et al. 2020; Schmidt et al. 2021) and with additional mapping at the pore center of wheat germ agglutinin (Gwosch et al. 2020; Thevathasan et al. 2019), which is a lectin known to inhibit the nuclear transport by binding and aggregating at the cytoplasmic face of the nuclear pores. Dual-color simultaneous mapping is obtained by exploiting the possibility to spectrally separate the emission from different fluorophores that can be excited by the same donut laser line, while photons are collected by two detectors tuned on different spectral windows. The result is rendered as "dcr" (detector channel ratio), representing the ratio of emission events detected around 680 nm wavelength

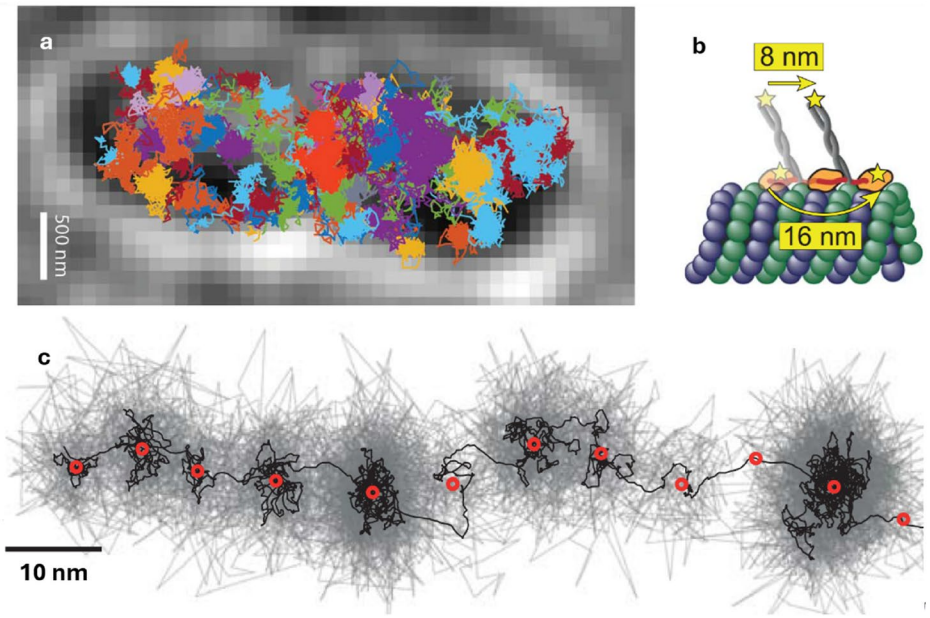

FIGURE 3 | Examples of MINFLUX tracking: (a) 77 trajectories (in different colors) of 30S ribosomal subunit proteins in a E.coli cell (reproduced with permission from (Balzarotti et al. 2017)). (b) model of kinesin hand-over-hand walk and (c) long-term (10 s) trajectory of a single kinesin on microtubule (scale bar: 10 nm, black line: 20 ms running mean displacements), (reproduced with permission from (Deguchi et al. 2023)); more recently (Wirth et al. 2023; Wirth et al. 2024), the occurrence of 8 nm long steps instead of the full 16 nm ones has been ascribed to a different type of step, called chasse-inchworm, with the trailing foot following the leading one without overcoming (instead of the explanation suggested in (b), of different position for the labeling, at stem instead of foot).

to those at 640 nm, and then segmenting the so-obtained gray-scale image to a two-color only one (Abberior n.d.-a). Of course, the MINFLUX can have different donut-shaped excitation laser beam lines to be used, depending on the fluorophores to be localized. DNA-PAINT is one approach alternative to the blinking buffer one, which has also made NPC sub-units imaging possible (Schlichthaerle et al. 2019) (see Appendix A).

In addition to imaging static samples, microscopy—when fast enough—also allows to follow moving samples, which is definitely a case of interest in the life sciences for experiments on living systems. Whereas in vivo experiments pose additional challenges of sample stability that are difficult to overcome, at least in vitro experiments on living cells can be addressed routinely.

3 | MINFLUX Tracking Capabilities

An application of MINFLUX alternative to nanoscale imaging (nanoscopy) and, probably, even more promising, is that of tracking single molecules. Typically, in this implementation, some localization precision is traded in (accepting values up to ~20 nm) to gain, instead, in terms of localization time and finally tracking speed. This allows for following in live cells, for example, lipids or membrane proteins moving with a few 100 μs step, that is, almost 100× faster than with cameras, which is the most common approach. The first example of MINFLUX tracking was given in the original paper of Balzarotti et al., where the trajectories of 30S ribosomal subunit proteins inside an *E. coli* bacterial cell were reconstructed (Balzarotti et al. 2017) (see Figure 3a). Lipids diffusing through a lipid-bilayer model of cell membrane were tracked instead in (Gwosch et al. 2020). More recently, the famous walk of kinesin along microtubules has also been imaged and characterized for its specific mechanism by Deguchi et al. (Deguchi et al. 2023; Wirth et al. 2023) (see Figure 3b,c).

4 | MINFLUX Requirements

In addition to the dedicated high-quality electronics and search software algorithms workflow, the powerful MINFLUX technique poses some stringent requirements as for both sample preparation and environmental conditions. First, for nanoscopy imaging, the samples have to be very still. To this goal, an active piezoelectric stabilization is run against thermal drift, keeping the field of view position displacement below 1 nm. This is done thanks to fiducial gold beads used as a reference, which are tracked and kept in the same position by a closed-loop feedback on the piezo (this system being similar to the closed-loop mechanical scan correction of piezo actuators used for sample scan in atomic force microscopy since the early 2000s). Obviously, this requirement means that usually only chemically fixed samples are imaged at the highest resolution. In fact, for live-cell imaging, the fiducial gold beads have to be immobilized on the substrate before cell culture—or other types of fiducial markers have to be used—while the cells themselves can move several hundreds nm within imaging time.

A second requirement is for fluorescent tags (labels), which have to be physically as small as possible to guarantee the expected nm-scale super-resolution. Therefore, conventional indirect immunofluorescence is usually not appropriate in this respect, as in that case the average distance between the fluorophore label and actual imaging target can be as long as 20 nm, making the localization precision ineffective (see Figure 4), so-called

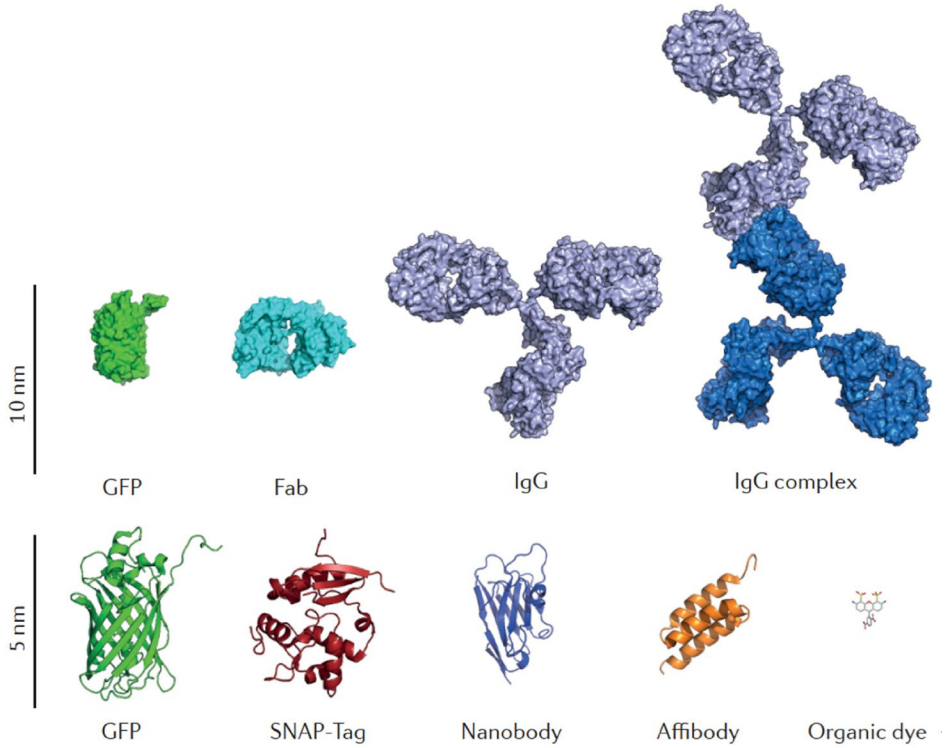

FIGURE 4 | Images representing the relative size of different fluorophore labels and constructs ensuring their binding to the targets of interest (reproduced with permission from (Sahl, Hell, and Jakobs 2017), structures come from the protein data bank).

linkage-error (Grabner et al. 2022). In fact, small-molecule probes or protein tags are used to enable imaging of nanoscale structures, and, for example, nanobodies are synthesized for use in this case in place of traditional antibodies (Sahl et al. 2023).

Additional requirements are those common to other localization microscopy techniques (Deschout et al. 2014) and already pointed out previously, namely fluorophores in the sample should be separated over time—by, for example, blinking, which is mainly ensured by using a properly formulated blinking buffer—and samples should be labeled at the appropriate density, that is, neither too low, which will not guarantee full reconstruction of the target object shape, nor too dense, which would eventually result in cross-talk at any given time instant. Detailed practical considerations on sample preparation are provided in Appendix A.

It is due to these significant requisites on experiment design and sample preparation that, so far, the best demonstrations of the possible high performance of MINFLUX have been mostly limited to imaging of well-characterized biological systems (e.g., the already mentioned NPCs or molecular rulers (Sahl et al. 2023)) and tracking of molecules with already partly known behavior (kinesin (Deguchi et al. 2023; Wirth et al. 2023; Wirth et al. 2024)).

5 | Sample Preparation Approaches

To have the fluorophore labels emitting separately in time be sparse enough in space and still silent ones being so densely present to finally allow for the whole picture to be built (at resolution better or comparable to the localization precision), different strategies can be pursued. For example, in a standard blinking-buffer approach as also used for STORM (such as adopted for the fixed cells shown in Figure 2), organic fluorophores are immersed in a buffer with reagents that enable the switching between fluorescent and non-fluorescent state. The commonly used buffer, containing glucose oxidase, is called GLOX. The GLOX buffer is prepared shortly before imaging, starting from a tris(hydroxymethyl)aminomethane (TRIS) buffer (containing 50 mM TRIS/HCl, 10 mM NaCl, 10% w/v glucose, pH 8.0), which is very stable and can last on the shelf for years. To this buffer, the solutions of enzymes as detailed in Appendix A are added, which can be prepared and stored in the fridge (4°C) for few weeks. β-mercaptoethylamine (MEA) thiols are also added as blinking compound (Lampe et al. 2012), which should come from an aliquot of the stock solution previously frozen that can be used only for up to 1 week after melting.

The thiol acts as a reducing agent for the fluorophore, converting it to non-fluorescent (dark state). The back-conversion to the fluorescent state may either occur spontaneously after some time or be induced by UV light (photoactivation), making the stochastic process somewhat tunable. The GLOX buffer is an oxygen scavenging system used to reduce the risk of bleaching and to favor long-lived triplet states, allowing the blinking to be controlled by the combination of the amount of MEA (bringing to a dark state) and UV exposure (bringing to a bright state). This GLOX-MEA approach has shown success for a number of traditional fluorophores, such as AlexaFluor 647 or other carbocyanine-based dyes, typically excited at 640 nm wavelength, for example, CF660C, CF680, or sCy5.

PALM-like photoconvertible proteins can also be used to exchange between OFF and ON states in a controlled way, such as the case for mMaple, adopted as well for imaging NPCs in

(Gwosch et al. 2020). This approach is especially useful for tracking experiments, where spontaneous fluorophore blinking is undesirable and, on the contrary, photostable and bright fluorophores are desirable not to lose the moving target (e.g., ATTO647N, abberior STAR RED, JFX650, JF646, mEOS3.2) (Abberior n.d.-b). In this application, even quantum dots fluorescing at the appropriate wavelength can, in principle, be used.

Another route to get the stochastic blinking of the fluorophores is the DNA-PAINT approach (Ostersehlt et al. 2022). This method uses binding and unbinding kinetics equilibrium of short oligonucleotides, instead of manipulating the fluorophore photophysics, that is, making it blink. The target is labeled with a docking strand that is complementary to another one holding the fluorophore. Same as in case of tracking, the fluorophore should be stable and bright here. Dyes often used in this method are Atto655 and Cy3B.

Additional methods have emerged, based on enzymatic labels, so-called self-labeling enzymes, namely SNAP-tag (Keppler et al. 2004) or HaloTag (Los et al. 2008). Both methods were demonstrated for example in (Scalisi, Pisignano, and Cella Zanacchi 2023) for imaging of NPCs based on labeling nucleoporin Nup96 in the nuclei of U2OS cells. In short, the tag is a specific functionalization of the protein of interest, which allows for easy binding of an appropriately engineered fluorophore. Several genetically encoded tags exist for fluorescence microscopy today (Liss et al. 2015). SNAP-tag can also be coupled for dual-color with CLIP-tag, which specifically reacts with orthogonal substrates.

Still, new solutions are expected in the future thanks to the click-chemistry. Finally, even spontaneous blinking fluorophores exist, which need neither a reducing buffer nor action of light to be activated, but this is presently limited to rare cases such as that of HM-SiR (Gerasimaitė et al. 2021).

In any case, each labeling strategy should consider the size of the fluorophore label and the distance between the label and target likely occurring in the labeled sample (see Figure 4). In there, nanobodies (nb) are listed as a possible alternative to traditional, large antibodies (Ab). A nb is nothing else than a smaller unit working as an Ab, namely a single-domain recombinantly-produced antigen binding protein or Ab fragment.

6 | Recent MINFLUX Applications in the Life Sciences

A number of different nanoscopy investigations in biology have been recently made viable by MINFLUX (van den Berg et al. 2023; Binotti et al. 2024; Jackson et al. 2022; Pape 2009; Wolff et al. 2020; Stephan et al. 2019; Carsten et al. 2023; Gürth et al. 2023). Among the many, our personal list of particularly notable ones includes the following examples.

In molecular neurobiology, Grabner et al. (Grabner et al. 2022) have used MINFLUX in 3D to resolve the molecular morphology of rod photoreceptor pre-synaptic active zone, where transmitter is released on fusion of synaptic vesicle. In that study also a special sample immobilization technique was implemented, called heat-assisted rapid de-hydration to allow a thin layer of rod synaptic terminals (spherules) being transferred onto glass substrate from retinal slices. The active zones were labeled by immunostaining, and the shape of the molecular complex at the release site was mapped with nanometer precision for the first time.

Another notable application of MINFLUX was carried out by Clowsley et al. (Clowsley et al. 2024), who investigated successfully the distribution in HEK293 cells and mouse cardiac myocytes of cardiac type 2 ryanodine receptor (RyR2). This large homotetramer (~560 kD) represents the molecular pathway through which most Ca^{2+} enters the cytosol during cardiac activation. Since the process of Ca release is in turn Ca-induced and locally regenerative, characterizing the distribution of RyR2 is of great interest. The authors used single-domain Ab against fluorescent protein domains engineered in RyR2 protein fusions and could map RyR2 subunits with 3 nm precision in 3D, allowing to understand also the molecular complex orientation in space. The obtained information was critically compared with electron microscopy data.

Finally, we would like to cite the work of Mulhall et al. (Mulhall et al. 2023), who observed the conformational states of PIEZO1. This protein belongs to a class of mechanosensitive ion channels that convert force into chemical and/or electrical signals. Whereas it is supposed that this occurs by deformation of its large propeller-like three blades of transmembrane domains, the actual mechanism of this transduction is not fully clarified. The authors observed in direct space the morphological modifications of working PIEZO1 in action, correlating it with channel activation, in native environment. Detection of conformational changes down to single nm resolution was possible using the MINFLUX. Good agreement with both cryo-EM and AI-based simulation tools (AlphaFold II) results was found.

7 | Perspectives

Similar 3D resolution as the MINFLUX can be obtained by other single-molecule localization systems such as the 4Pi; however, this comes at the cost of much more complex operation, due to the required work with two opposing objectives (Wang et al. 2021). Also, the current commercial implementation of MINFLUX actually comes after a complex combination of hardware and software systems, which obviously means high cost of the setup (in the order of 1 M€) and consequently still low overall accessibility. However, researchers are working on the development of a possible future simplified open-source setup (see, e.g., (Deguchi and Ries 2024)).

One current limitation of MINFLUX is in multi-color imaging. For example, for dual-color, to avoid the complex duplication of the scanning-localizing procedure with two different excitation lines, the two colors are obtained on emission by two fluorophores that can be excited by the same laser line and still have emission spectra different enough to allow for spectral separation. These “color” maps are obtained by rendering the previously mentioned parameter dcr, representing the fraction of photon counts for each spectral detection window (see, e.g., (Remmel et al. 2024)). This approach can be used, for example, for the pairs of fluorophores abberior FLUX 640 and FLUX 680, or CF680 and sCy5.

It is also partly due to this limitation, as well as the continuously improved localization precision also occurring for other single-molecule localization microscopy techniques, that it is a general feeling in the community that MINFLUX will be more likely used in the future mainly in tracking experiments rather than for nanoscopy of static samples. For example, a new promising technique, apparently a variant of MINFLUX according to the name yet more similar to STED, is MINSTED (Weber et al. 2021, 2023). In MINSTED the donut is used again for depletion instead of excitation, same as in STED, but the raster scan of STED is combined with a local circular scan of the depletion donut, coupled with subsequent displacement toward the position on the circle where photon detection occurs, together with progressive donut shrinking, pretty much in the fashion of MINFLUX. This approach may reach similar single-nm resolution levels than MINFLUX, thanks to the donut being used not much to separate fluorophores at small distances but rather to establish the fluorophore's position. In addition, the requested photon budget is lower than for standard STED or STORM (Weber et al. 2021).

Another advancement, possibly obtained by combining different optical techniques, may be represented by two-photon MINFLUX (Zhao et al. 2022). This variant holds promise for doubling localization precision in 3D thanks to non-linear effects, requiring only ¼ photon budget as standard MINFLUX.

Clearly, significant progress is expected on a monthly base thanks to the continuous effort made by companies at synthesizing more and more fluorophore systems specifically designed for localization microscopy and especially MINFLUX (Wang et al. 2023; de Beer and Giepmans 2020; Prakash 2022). The future is obviously "bright" for this non-invasive, high-precision technique, and other nanoscopies, when appropriate biological questions will be addressed by the scientific community.

Author Contributions

Marco Salerno: writing – original draft, methodology, writing – review and editing. **Alberto Diaspro:** conceptualization, funding acquisition, writing – review and editing, supervision. **Kimiya Pakravanan:** writing – review and editing. **Elena Angeli:** writing – review and editing, validation. **Virginia Bazzurro:** methodology, investigation, writing – review and editing. **Mohammadmehdi Roushenas:** writing – review and editing. **Paolo Bianchini:** writing – review and editing.

Acknowledgments

We thank Clara Gürth of Abberior for her suggestions for manuscript revision and constant support in use of our MINFLUX system. SEELIFE ("StrEngthEning the ItaLIan InFrastructure of Euro-bioimaging") was funded by the European Union—Next Generation EU PNRR MUR Infrastructure program (B53C22001810006, IR0000023). Thanks to this project, a commercial MINFLUX has been installed in October 2023 at the Genoa site of the Italian Advanced Light Microscopy node of Eurobioimaging.

Data Availability Statement

The data that support the findings of this study are available from the corresponding author upon reasonable request.

References

Abberior. n.d.-a courtesy of Gürth C., "Guide to Minflux Sample Preparation."

Abberior. n.d.-b courtesy of Gürth, C. "GLOX-MEA Preparation Protocol."

Abberior. n.d. "Imspector manual—Version for Minflux."

Balzarotti, F., Y. Eilers, K. C. Gwosch, et al. 2017, Science. "Nanometer Resolution Imaging and Tracking of Fluorescent Molecules With Minimal Photon Fluxes." 355: 606–612.

Bianchini, P., C. Peres, M. Oneto, S. Galiani, G. Vicidomini, and A. Diaspro. 2015. "STED Nanoscopy: A Glimpse Into the Future." *Cell and Tissue Research* 360: 143–150. https://doi.org/10.1007/s00441-015-2146-3.

Binotti, B., M. Ninov, A. P. Cepeda, et al. 2024. "ATG9 Resides on a Unique Population of Small Vesicles in Presynaptic Nerve Terminals." *Autophagy* 20, no. 4: 883–901. https://doi.org/10.1080/15548627.2023.2274204.

Carsten, A., M. Rudolph, T. Weihs, et al. 2023. "MINFLUX Imaging of a Bacterial Molecular Machine at Nanometer Resolution." *Methods and Applications in Fluorescence* 11, no. 1: 15004. https://doi.org/10.1088/2050-6120/aca880.

Cella Zanacchi, F., Z. Lavagnino, M. Perrone Donnorso, et al. 2011. "Live-Cell 3D Super-Resolution Imaging in Thick Biological Samples." *Nature Methods* 8, no. 12: 1047–1050. https://doi.org/10.1038/nmeth.1744.

Clowsley, A. H., A. Meletiou, E. Lučinskaitė, et al. 2024. "Analysis of RyR2 Distribu2on in HEK293 Cells and Mouse Cardiac Myocytes Using 3D MINFLUX Microscopy." https://doi.org/10.1101/2023.07.26.550636.

de Beer, M. A., and B. N. G. Giepmans. 2020. "Nanobody-Based Probes for Subcellular Protein Identification and Visualization." *Frontiers in Cellular Neuroscience* 14: 573278. https://doi.org/10.3389/fncel.2020.573278.

Deguchi, T., M. K. Iwanski, E. M. Schentarra, et al. 2023. "Direct Observation of Motor Protein Stepping in Living Cells Using MINFLUX." *Science* 379, no. 6636: 1010–1015. https://doi.org/10.1126/science.ade2676.

Deguchi, T., and J. Ries. 2024. "Simple and Robust 3D MINFLUX Excitation With a Variable Phase Plate." *Light: Science & Applications* 13, no. 1: 134. https://doi.org/10.1038/s41377-024-01487-1.

Deschout, H., F. C. Zanacchi, M. Mlodzianoski, et al. 2014. "Precisely and Accurately Localizing Single Emitters in Fluorescence Microscopy." *Nature Methods* 11: 253–266. https://doi.org/10.1038/nmeth.2843.

Diaspro, A. (Ed.). 2010. *Nanoscopy and Multidimensional Optical Fluorescence Microscopy*. Chapman and Hall/CRC.

Diaspro, A., and P. Bianchini. 2020. "Optical nanoscopy." *La Rivista del Nuovo Cimento* 43: 385–455. https://doi.org/10.1007/s40766-020-00008-1.

Diaspro, A., and van Zandvoort, M. A. M. J. (Eds.). 2021. *Super-Resolution Imaging in Biomedicine*. CRC Press.

Galiani, S., B. Harke, G. Vicidomini, et al. 2012. "Strategies to Maximize the Performance of a STED Microscope." *Optics Express* 20, no. 7: 7362–7374. https://doi.org/10.1364/oe.20.007362.

Gerasimaitė, R. T., J. Bucevičius, K. A. Kiszka, et al. 2021. "Blinking Fluorescent Probes for Tubulin Nanoscopy in Living and Fixed Cells." *ACS Chemical Biology* 16, no. 11: 2130–2136. https://doi.org/10.1021/acschembio.1c00538.

Grabner, C. P., I. Jansen, J. Neef, et al. 2022. "Resolving the molecular architecture of the photoreceptor active zone with 3D-MINFLUX." *Science Advances*. 8, no. 28: eabl7560 1–12. https://doi.org/10.1126/sciadv.abl7560.

Gürth, C.-M., M. Augusta, V. M. Palacios, et al. 2023. "Neuronal Activity Modulates the Incorporation of Newly Translated PSD-95 Into a Robust Structure as Revealed by STED and MINFLUX." https://doi.org/10.1101/2023.10.18.562700.

Gwosch, K. n.d. “It Cannot Get Sharper.” https://www.mpinat.mpg.de/652475/pr_1639.

Gwosch, K. C., J. K. Pape, F. Balzarotti, et al. 2020. “MINFLUX nanoscopy delivers 3D multicolor nanometer resolution in cells.” *Nature Methods* 17, no. 2: 217–224. https://doi.org/10.1038/s41592-019-0688-0.

Hell, S. W., and J. Wichmann. 1994. “Breaking the Diffraction Resolution Limit by Stimulated Emission: Stimulated-Emission-Depletion Fluorescence Microscopy.” *Optics Letters* 19: 780–782. https://doi.org/10.1364/OL.19.000780.

Jackson, V., J. Hermann, C. J. Tynan, et al. 2022. “The Guidance and Adhesion Protein FLRT2 Dimerizes in Cis via Dual Small-X3-Small Transmembrane Motifs.” *Structure* 30, no. 9: 1354–1365.e5. https://doi.org/10.1016/j.str.2022.05.014.

Keppler, A., H. Pick, C. Arrivoli, H. Vogel, and K. Johnsson. 2004. “Labeling of Fusion Proteins With Synthetic Fluorophores in Live Cells.” www.pnas.orgcgidoi10.1073pnas.0401923101.

Lampe, A., V. Haucke, S. J. Sigrist, M. Heilemann, and J. Schmoranzer. 2012. “Multi-Colour Direct STORM With Red Emitting Carbocyanines.” *Biology of the Cell* 104, no. 4: 229–237. https://doi.org/10.1111/boc.201100011.

Liss, V., B. Barlag, M. Nietschke, and M. Hensel. 2015. “Self-Labelling Enzymes as Universal Tags for Fluorescence Microscopy, Super-Resolution Microscopy and Electron Microscopy.” *Scientific Reports* 5, no. 17740: 1–13. https://doi.org/10.1038/srep17740.

Los, G. V., L. P. Encell, M. G. McDougall, et al. 2008. “HaloTag: A Novel Protein Labeling Technology for Cell Imaging and Protein Analysis.” *ACS Chemical Biology* 3, no. 6: 373–382. https://doi.org/10.1021/cb800025k.

Lukinavičius, G., J. Alvelid, R. Gerasimaitė, et al. 2024. “Stimulated Emission Depletion Microscopy.” *Nature Reviews Methods Primers* 4, no. 1: 56. https://doi.org/10.1038/s43586-024-00335-1.

Mulhall, E. M., A. Gharpure, R. M. Lee, et al. 2023. “Direct Observation of the Conformational States of PIEZO1.” *Nature* 620, no. 7976: 1117–1125. https://doi.org/10.1038/s41586-023-06427-4.

Ostersehlt, L. M., D. C. Jans, A. Wittek, et al. 2022. “DNA-PAINT MINFLUX nanoscopy.” *Nature Methods* 19, no. 9: 1072–1075. https://doi.org/10.1038/s41592-022-01577-1.

Owen, D. M., M. Sauer, and K. Gaus. 2012. “Fluorescence Localization Microscopy: The Transition From Concept to Biological Research Tool.” *Communicative & Integrative Biology* 5, no. 4: 345–349. https://doi.org/10.4161/cib.20348.

Pape, J. K. 2009. “Contributed New Reagents/Analytic Tools.” *PNAS* 117, no. 34: 20607–20614. https://doi.org/10.1073/pnas.2009364117/-/DCSupplemental.

Petrovic, S., D. Samanta, T. Perriches, et al. 2022. “Architecture of the Linker-Scaffold in the Nuclear Pore.” *Science* 376: eabm9798. https://doi.org/10.1126/science.abm9798.

Prakash, K. 2022. “At the Molecular Resolution With MINFLUX?” *Philosophical Transactions of the Royal Society A: Mathematical, Physical and Engineering Sciences* 380, no. 2220: 20200145. https://doi.org/10.1098/rsta.2020.0145.

Remmel, M., J. Matthias, R. Lincoln, et al. 2024. “Photoactivatable Xanthone (PaX) Dyes Enable Quantitative, Dual Color, and Live-Cell MINFLUX Nanoscopy.” *Small Methods* 8: e2301497. https://doi.org/10.1002/smtd.202301497.

Sahl, S. J., S. W. Hell, and S. Jakobs. 2017. “Fluorescence Nanoscopy in Cell Biology.” *Nature Reviews Molecular Cell Biology* 18: 685–701. https://doi.org/10.1038/nrm.2017.71.

Sahl, S. J., J. Matthias, K. Inamdar, et al. 2023. “Direct Optical Measurement of Intra-Molecular Distances Down to the Ångström Scale.” https://doi.org/10.1101/2023.07.07.548133.

Salerno, M., and V. Bazzurro. n.d. “PNRR SEELIFE Project at UniGE-DiFi.” https://www.difi.unige.it/en/research/applied-physics/biophysics/nanoscale-biophyiscs-nanoscopy/seelife.

Scalisi, S., D. Pisignano, and F. Cella Zanacchi. 2023. “Single-Molecule Localization Microscopy Goes Quantitative.” *Microscopy Research and Technique* 86, no. 4: 494–504. https://doi.org/10.1002/jemt.24281.

Schlichthaerle, T., M. T. Strauss, F. Schueder, et al. 2019. “Direct Visualization of Single Nuclear Pore Complex Proteins Using Genetically-Encoded Probes for DNA-PAINT.” *Angewandte Chemie International Edition* 58, no. 37: 13004–13008. https://doi.org/10.1002/anie.201905685.

Schmidt, R., T. Weihs, C. A. Wurm, et al. 2021. “MINFLUX Nanometer-Scale 3D Imaging and Microsecond-Range Tracking on a Common Fluorescence Microscope.” *Nature Communications* 12, no. 1: 1478. https://doi.org/10.1038/s41467-021-21652-z.

Stephan, T., A. Roesch, D. Riedel, and S. Jakobs. 2019. “Live-cell STED nanoscopy of mitochondrial cristae.” *Scientific Reports* 9, no. 1: 12419. https://doi.org/10.1038/s41598-019-48838-2.

Thevathasan, J. V., M. Kahnwald, K. Cieśliński, et al. 2019. “Nuclear Pores as Versatile Reference Standards for Quantitative Superresolution Microscopy.” *Nature Methods* 16, no. 10: 1045–1053. https://doi.org/10.1038/s41592-019-0574-9.

van den Berg, C. M., V. A. Volkov, S. Schnorrenberg, et al. 2023. “CSPP1 Stabilizes Growing Microtubule Ends and Damaged Lattices From the Luminal Side.” *Journal of Cell Biology* 222: e202208062. https://doi.org/10.1083/jcb.202208062.

Vicidomini, G., P. Bianchini, and A. Diaspro. 2018. “STED Super-Resolved Microscopy.” *Nature Methods* 15: 173–182. https://doi.org/10.1038/nmeth.4593.

Wang, J., E. S. Allgeyer, G. Sirinakis, et al. 2021. “Implementation of a 4Pi-SMS Super-Resolution Microscope.” *Nature Protocols* 16, no. 2: 677–727. https://doi.org/10.1038/s41596-020-00428-7.

Wang, J., Z. Zhang, H. Shen, Q. Wu, and M. Gu. 2023. “Application and Development of Fluorescence Probes in MINFLUX Nanoscopy.” *Journal of Innovative Optical Health Sciences* 16: 2230011. https://doi.org/10.1142/S1793545822300117.

Weber, M., M. Leutenegger, S. Stoldt, et al. 2021. “MINSTED Fluorescence Localization and Nanoscopy.” *Nature Photonics* 15, no. 5: 361–366. https://doi.org/10.1038/s41566-021-00774-2.

Weber, M., H. von der Emde, M. Leutenegger, et al. 2023. “MINSTED Nanoscopy Enters the Ångström Localization Range.” *Nature Biotechnology* 41, no. 4: 569–576. https://doi.org/10.1038/s41587-022-01519-4.

Wirth, J. O., L. Scheiderer, T. Engelhardt, et al. 2023. “MINFLUX dissects the unimpeded walking of kinesin-1.” *Science 379*, no. 6636: 1004–1010. https://doi.org/10.1126/science.ade2650.

Wirth, J. O., E. M. Schentarra, L. Scheiderer, V. Macarrón-Palacios, M. Tarnawski, and S. W. Hell. 2024. “Uncovering Kinesin Dynamics in Neurites With MINFLUX.” *Communications Biology* 7, no. 1: 661. https://doi.org/10.1038/s42003-024-06358-4.

Wolff, G., R. W. A. L. Limpens, J. C. Zevenhoven-Dobbe, et al. 2020. “A molecular pore spans the double membrane of the coronavirus replication organelle.” *Science 369*, no. 6509: 1395–1398. https://doi.org/10.1126/science.abd3629.

Xiao, J., and T. Ha. 2017. “Flipping Nanoscopy on Its Head.” *American Association for the Advancement of Science* 355: 581–582. https://doi.org/10.1126/science.aam6589.

Zhao, K., X. Xu, W. Ren, D. Jin, and P. Xi. 2022. “Two-Photon MINFLUX With Doubled Localization Precision.” *eLight* 2, no. 1: 1–10. https://doi.org/10.1186/s43593-021-00011-x.

Appendix A

Imaging method details for the NPCs sample in Figure 2

Same as in a typical sample preparation procedure, 18–25 mm diameter coverslips (#1.5 or #1.5H for the thickness) can be used as the substrates for the biological sample (e.g., cultured cells). For piezo stabilization, 100 μL of 150 nm diameter fiducial gold beads (at a stock solution concentration of 3.6 10^9 particles/mL) are added and let to adsorb for typically 5 min at room temperature. Then, the gold beads solution is discarded and the coverslip is rinsed with phosphate buffer saline (PBS) three times.

The blinking buffer used in this case was prepared by adding to the GLOX buffer the following concentrations of the respective solutions: 0.064 g/L catalase (stock solution: 20 g/L in Milli-Q water, prepared from powder); 0.4 g/L glucose oxidase (stock solution: 70 g/L in TRIS buffer without glucose); 10–30 mM MEA (stock solution: 1 m in PBS, prepared from powder). Variability in the amount of MEA is key to proper sample working. A cavity microscope slide is then filled with 70 μL GLOX buffer and the coverslip with sample is then placed upside-down onto the filled cavity such as to avoid any air bubbles. The edge is sealed against diffusion of oxygen from ambient air with silicone-based two-component elastomeric products used for dental impression replicas, for example, Picodent or Twinsil (Gürth et al. 2023).

European Biophysics Journal
https://doi.org/10.1007/s00249-025-01770-y

ORIGINAL ARTICLE

Image analysis tools for improved characterization of nuclear chromatin patterns by confocal fluorescence microscopy

Mohammadmehdi Roushenas[1] · Marco Salerno[1] · Virginia Bazzurro[1] · Elena Gatta[1] · Alberto Diaspro[1,2]

Received: 30 January 2025 / Revised: 18 April 2025 / Accepted: 22 April 2025

Abstract

We have collected fluorescence images of fixed cell nuclei of two different types—HeLa and HepG2—with DNA labeled by a standard fluorophore, and have devised three different quantitative parameters aimed to describe the distribution of the nuclear chromatin. The parameters are the fractal dimension, associated with the intricacy and hierarchical structure of chromatin; the total perimeter of local maxima, associated with the amount of chromatin domains; and the radial distance of angularly averaged intensity profile maximum, associated with the possible occurrence of a peak density at a characteristic distance from the nucleus center. Our results suggested that it was possible to differentiate the two types of cells in the 3D space of the defined parameters. Therefore, these parameters appear promising in identifying specific functional patterns in chromatin. At the same time, the negative control of different runs of measurements on the same cell type also showed at least partial differentiation. Thus, the tool proposed here for nuclear chromatin pattern characterization is probably sensitive to the cell life cycle moment almost as much as to the cell type and should be tested further on cells synchronized at the same phase during their cycle.

Keywords Cell nuclei · Chromatin compaction · Confocal microscopy · Hoechst · Fractal dimension

Introduction

Pointing to the importance of chromatin is an easy task, supported by such a wide variety of literature background (Van Steensel 2011) (Mishra et al. 2023). In short, chromatin is a complex of nucleic acids and proteins responsible for packing genetic information in living cells and for its transfer to daughter cells. To this goal, the extraordinarily long DNA chain in humans (almost two meters) is packed in the 10 µm-scale size of the cell nucleus in such a way that it is still ready to be unzipped and accessed for replication at the right moment (Kak 2023). The chromatin structure presents multiple organization levels, spanning from micrometer down to nanometer scale (Mirny 2011), from the single DNA chain size, wrapped around histones octamers to form nucleosome spools, to the bead-on-a-string chromatin fiber in the scale of 10 nm. Nowadays, even the lower levels are accessible thanks to super-resolution microscopy (Kostiuk et al. 2019) (Benke and Manley 2012) (Burgers and Vlijm 2023) (Lakadamyali and Cosma 2015)(Burgers and Vlijm 2023) (Pierzynska-Mach, Czada, et al., 2023b), which can primarily be used for addressing specific interactions occurring in live cells during transcription, translation and even repair of DNA. Therefore, the relevance of a study based on imaging with diffraction-limited resolution (as large as at least 200 nm) by simple confocal microscopy could be questioned. However, the size scale of the chromatin structure is already known, mainly after cryo-electron microscopy studies (Takizawa and Kurumizaka 2022), and the closest higher level has also been clarified by small-angle X-ray scattering (SAXS) studies (Nishino et al. 2012). For example, more than one decade ago, the latter technique made it possible to clarify about the hypothesized existence of a higher level of chromatin fibers in the size scale of 30 nm, concluding that there is not necessarily such a regular structure in human mitotic chromosomes (Hansen 2012). Nishino et al. also investigated the size range of 50–1000 nm by ultra-SAXS, showing that no regular structures are present in human mitotic chromosomes even on that scale (Nishino

✉ Marco Salerno
marco.salerno@unige.it

[1] Dipartimento Di Fisica, Università Di Genova, Genoa, Italy

[2] Nanoscopy and NIC@Iit, CHT, Istituto Italiano Di Tecnologia, Genoa, Italy

et al. 2012). On the other hand, with chromatin not really being regular, yet somewhat hierarchically arranged in an efficient way to allow for its high level of compaction, over the years several researchers have put forward the hypothesis of a fractal arrangement extending in the submicrometric size scale. In this intermediate mesoscale size, chromatin structure analysis falls under the domain of confocal microscopy. Therefore, we have tried to use this imaging technique to investigate chromatin organization, as we think that, even on such a relatively large scale across the micrometer, chromatin organization still has to disclose helpful information. This has already been observed in the past (Mascetti et al. 1996), yet should be reconsidered with current image analysis capabilities (see, e.g., Pierzynska-Mach, Cainero, et al. 2023a). Indeed, in this work, one of the parameters extracted from our images is the fractal dimension (FD). However, we have worked out two more parameters, trying to express both the level of chromatin density and its distribution with the distance from the nucleus center, namely the total perimeter of domains (TPD) of chromatin and the radial position of maximum density, R_{max}, respectively. The goal was to find a set of descriptors that will allow the distinction of chromatin arrangement between different cell types and, in perspective, also between healthy and diseased cell conditions.

The high complexity of the cell nucleus (Maraldi et al., 2003) goes along with chromatin organization. Investigations of chromatin distribution patterns started already several decades ago, by simple methods such as evaluation of optical density, which disclosed differences between cell types or functioning conditions (Durie et al. 1978; Sahota et al. 1986). More recently, changes in chromatin patterns of neurons were associated with developmental disorders (García-Cabezas et al. 2018). Our preliminary work was not intended to provide insights into the functional properties of this organization. Rather, we aim to suggest a tool for future studies correlating functional characterization with the structural distribution of chromatin, as observable in conditions not too far from native ones, by optical fluorescence microscopy.

Experimental

Sample preparation

Both cell types, namely HeLa and human hepatocellular carcinoma (HepG2) cell line, were cultured in 90% Dulbecco's modified Eagle's medium–high glucose (DMEM, Sigma-Aldrich, St. Louis, MO, USA, product No. D5796), 10% fetal bovine serum (Sigma-Aldrich, St. Louis, MO, USA, product No. F9665), 2.0 mM glutamine (Sigma-Aldrich, St. Louis, MO, USA, product No. G7513), and 100 IU/mL penicillin–streptomycin (Sigma-Aldrich, St. Louis, MO, USA, product No. P4333) and maintained at 37 °C in a humidified atmosphere of 95% air and 5% CO_2. The passage number of the cell cultures was eight for HeLa (P8) and seven for HepG2 (P7). The cells were plated at a density of 5.0–10 $\times 10^4$ cells on 18 mm diameter poly-L-lysine-coated glass coverslips (Sigma-Aldrich, St. Louis, MO, USA, product No. P2636). For the labeling, the cells were fixed with formaldehyde solution 4%, buffered, pH 6.9 (Sigma-Aldrich, St. Louis, MO, USA, product No. 1.00496) for 15 min at room temperature. After washing twice with Dulbecco's phosphate-buffered saline (DPBS, Sigma-Aldrich, St. Louis, MO, USA, product No. D8662), the cells were stained with 2.5 µM Hoechst (Sigma-Aldrich, St. Louis, MO, USA, product No. 14533) at room temperature for 30 min. Following three washes of 5 min each with DPBS, the coverslip was mounted on a microscope glass slide (1″ × 3″) with ProLong™ Glass Antifade (Thermo Fisher Scientific, product No. P36980).

Fluorescence microscopy imaging of cell nuclei

We used a confocal inverted microscope Stellaris 8 by Leica Microsystems (Mannheim, Germany), utilizing the doughnut-shaped laser for stimulated emission depletion (STED), with 775 nm wavelength, at maximum available intensity (100% power), for two-photon excitation (2PE) of Hoechst as the nuclei labeling fluorophore (see Discussion for more detailed considerations). For each sample, we collected several images (8-bit intensity scale) of different regions, each containing, in turn, several different nuclei (see Fig. 1a). The expected resolution in confocal mode was diffraction limited, i.e., around 250 nm in the xy focal image plane. Therefore, according to the Nyquist–Shannon rule (Diaspro and van Zandvoort 2021), we set a pixel size of 100 nm, a little less than half the expected resolution, which allowed us to cover several nuclei with a typical image digital size of 512 × 512 pixels.

Image analysis

The images, saved with the proprietary Leica software LasX, were then processed with Fiji distribution of ImageJ (Abràmoff et al. 2004) according to the protocols described next for each of the three parameters of interest to be extracted. The first step for all parameters was cropping the image (command *Image-Crop*) to isolate the single nucleus of interest; see, e.g., the rectangular region of interest (ROI, yellow edges) in Fig. 1a.

Fractal dimension, FD

The FD of the patterns inside the images of nuclei was obtained with a dedicated Fiji plugin, based on the

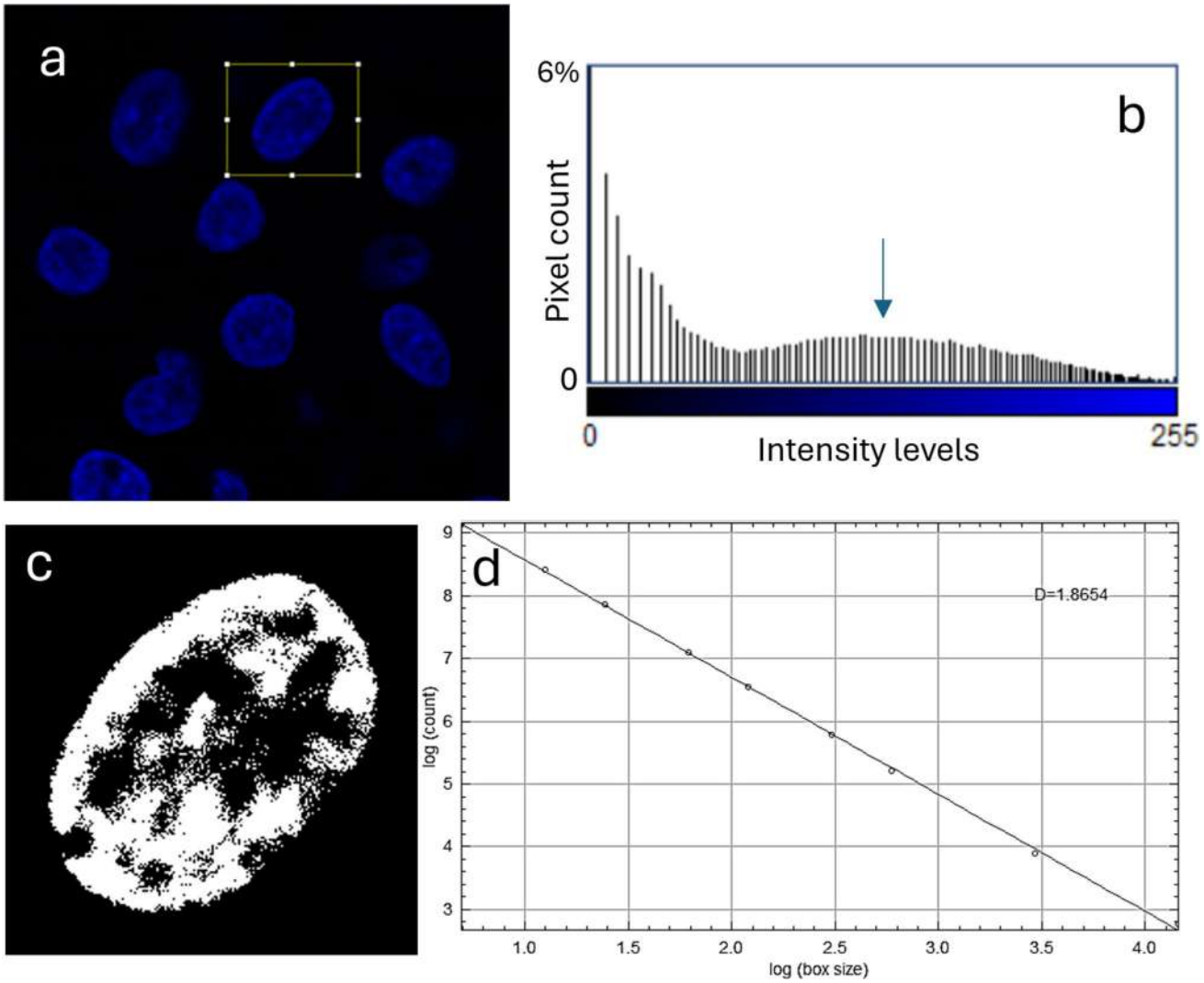

Fig. 1 Extraction of FD value. **a** Original image, with selection of ROI to be cropped. **b** Histogram of intensity levels obtained after equalization, used to find the threshold for binarization (see arrow). **c** Resulting binarized image. **d** Log–log plot of intensity versus box size, the slope is the FD

common method known as "box counting" (Russ 1994, 2011). After cropping, we first equalized the distribution of intensity levels (*Process-Enhance contrast*, *Equalize histogram*, with Saturated pixels set to 0.35%), such that its histogram appeared to be similar to that shown in Fig. 1b. Then, we binarized the image of the single-nucleus setting the manual threshold (*Image-Adjust-Threshold*) to the peak position of the intensity levels associated with the fluorophore (center of the broadband on the right side, see arrow in Fig. 1b). The result of this binarization was typically as shown in Fig. 1c. On this image, we applied command *Analyze-Tools-Fractal box count*, setting the Black background option. The result is a log–log plot, as shown in Fig. 1d, whose slope is the FD value.

Total perimeter of chromatin domains, TPD

In Fig. 2, the protocol used to extract parameter TPD from the nuclei images is shown. After cropping and equalizing the single-nucleus image, as in Fig. 1a, b, the image was first low-pass filtered by *Process-filters-Gaussian blur* with sigma radius 2 to remove possible noisy pixels. Then the edges of the high-intensity domains were identified by *Process-find edges*, which implements a Sobel filter for edge detection (basically, 2D derivative along major image axis x and y), see Fig. 2a (Russ 2011). Then, the image of edges was thresholded by *Image-adjust-threshold*, B&W option with dark background, setting the top range cursor in the middle (highest point) of the right band in the histogram.

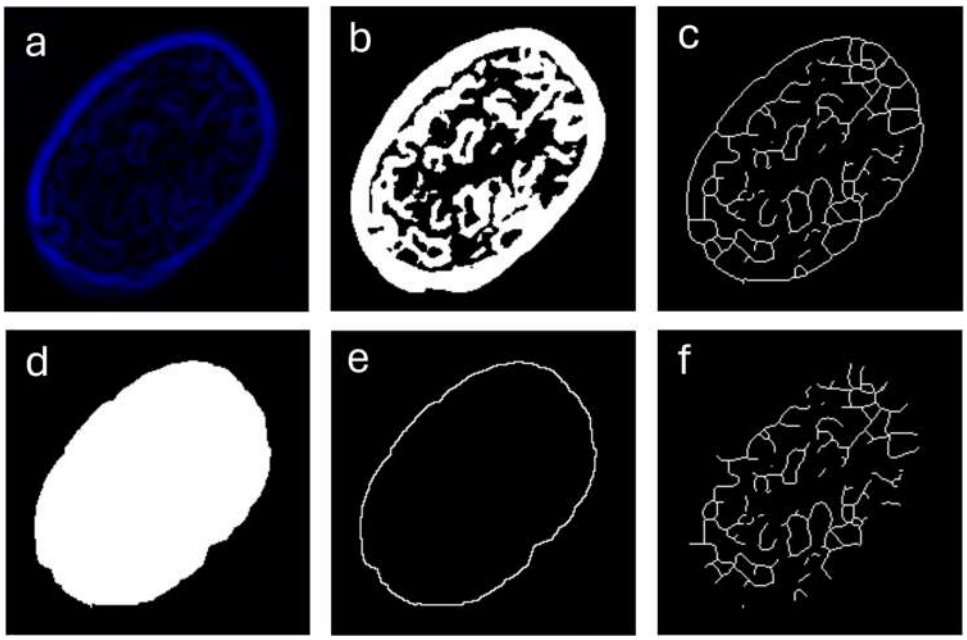

Fig. 2 Extraction of the TPD value. **a** Result of Sobel edge detection filter. **b** Same image as in (**a**), after binarization. **c** Result of skeletonization. **d** Same image as in (**b**) after filling holes operation. **e** Result of erosion of (**d**) by 1 pixel and outline detection. **f** Result of subtraction (**c**)-(**e**); the TPD is calculated after the total length of these white lines, divided by the nucleus area in (**d**) (for normalization purposes)

The so-binarized edges of the chromatin domains are shown in Fig. 2b. This image was then skeletonized by *Process-binary-skeletonize* (Fig. 2c). The whole nucleus area was obtained next by applying to the former stage image (Fig. 2b) the command *Process-binary-fill holes* (See Fig. 2d). The final goal was to isolate the nucleus outer edge, to be able to remove it from the inner chromatin domain edges. To this aim, the whole white image of the nucleus was eroded one pixel in width, by *Process-binary-erode*, and the outline was obtained by *Process-binary-outline*. Next, we used the *Process-image calculator* to subtract the last obtained outline (Fig. 2e) from the previous skeletonized image (Fig. 2c). We then went back to the filled nucleus image (Fig. 2d) and selected *Analyze-Set measurements*, *Area fraction*. With *Analyze-Measure*, the % Area of the rectangular image corresponding to the inner nucleus region was obtained and annotated. On the skeletonized image, again we applied *Analyze-Measure* and obtained the total length of chromatin domains. The TPD value was finally obtained by normalizing the latter value to the previous one obtained for the nucleus area, such as to remove the effect of nucleus size.

Radial position of maximum intensity, R_{max}.

In Fig. 3, the protocol used to extract parameter R_{max} from the nuclei images is shown. In particular, to determine this parameter, we discarded nuclei with clearly asymmetric shape (protrusions or dents), and considered only nuclei with roughly elliptical shape. Examples of the shapes of discarded nuclei have been shown in Fig.S3. After cropping and equalizing the single-nucleus image (Fig. 3a), the main axis of the—approximately—elliptical nucleus was aligned with the rectangular image axis by rotation, with *Edit-Selection-Rotate*. The following step consisted of a new cropping operation, aiming to select just the rectangle containing the nucleus and almost touching its edges; only 1 pixel outside the edge was maintained for the sake of avoiding any possible loss of information (see Fig. 3b). Then, we performed what we called a "circularization" of the nucleus, meaning that the shorter size of the rectangular image was stretched until it reached the same pixel size as the long one, by *Image-Adjust-Size*, (Fig. 3c; the "Keep aspect ratio" option was de-selected during this operation). Next, we applied the Fiji plugin Radial_class (Baggethun 2002). All the 360 profiles starting from the center of the image—and circularized nucleus—and pointing around each at 1° angular spacing were so averaged to provide a single profile (Fig. 3d). To compare the profiles from nuclei of different sizes, the x-axis in the plots (radial distance) was normalized for each profile to its maximum value, such that it then appeared to span the range from 0 to 1. At this point, we sought the x position at which the absolute maximum in the profile occurred, which was called R_{max}.

Plotting and statistical analysis

For the basic 1D graphic profiles, SciDAVis 2.7 was used (*SciDAVis Plotting Software*, n.d.). For 3D scattering plots in the space of chromatin describing parameters, we used SigmaPlot 12.0 (Grafiti, Palo Alto, CA, USA, (*SigmaPlot Web Page*, n.d.)). This software was also used for comparing the populations with one-way ANOVA; the Tukey's pair test was carried out, looking at different statistically significant levels for the differences, i.e., $p < 0.05$ (identified with a single star

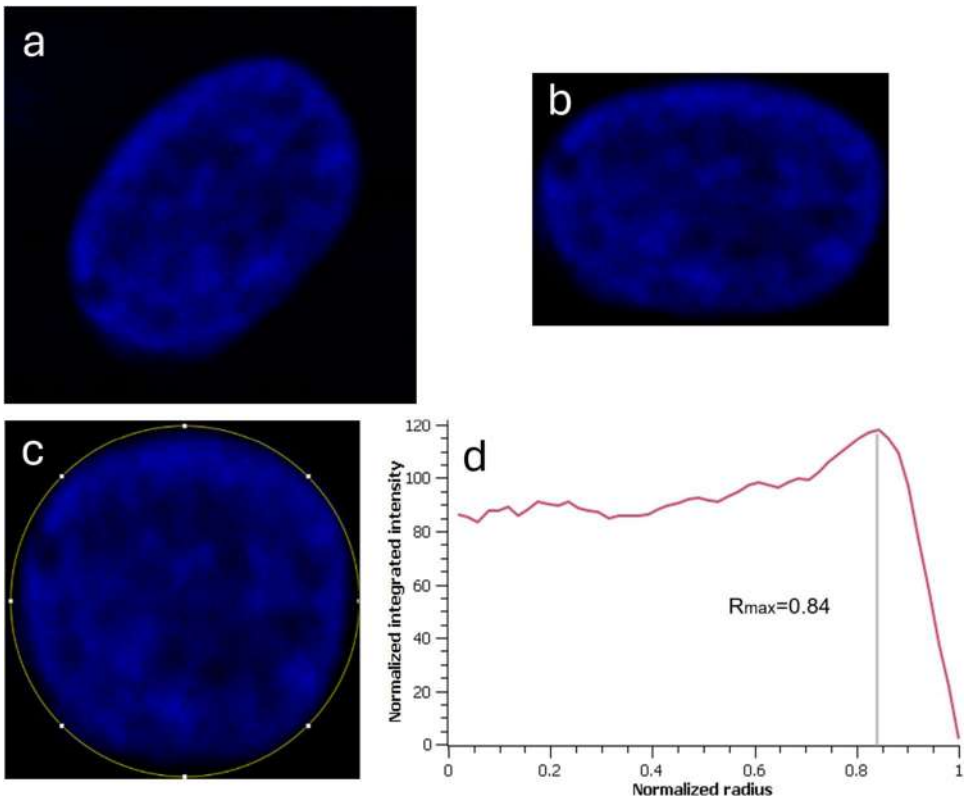

Fig. 3 Extraction of R_{max} value. **a** Typical image of a single nucleus after cropping. **b** The same nucleus as in (**a**) after rotation to align the main axis of the ellipsoidal nucleus to the horizontal and vertical axis of the image, and cropping further close to the nucleus edges (1 pixel background only). **c** Image after stretching the short side in (**b**) to the same size as the long side to make it square (nucleus circularization). **d** Mean radial profile averaged across all directions at 360° (step 1°) around the center of the circle in (**c**), with renormalization of circle radius to 1

symbol, *), $p < 0.01$ (two stars, **), and $p < 0.001$ (three stars, ***). For the 3D rendering with ellipsoidal volumes (Fig.S4), MATLAB R2023b was used (The MathWorks, Inc., Natick, MA, USA, (*MATLAB Web Page* 2023)).

Results

In Fig. 4a, the data resulting from the experiment called run#1 are reported to compare the two cell types, HeLa and HepG2. The images of the nuclei used to extract those data have been included as Fig.S1,2 for each cell type, separately. Clearly, on inspection of those images from a first sight by the naked eye, no significant difference emerges between the two populations, given the intra-population variability. Nevertheless, a deeper insight is expected based on the distribution of values for our three selected parameters.

In Fig. 4a, b, the 20 data points of each of the HeLa and HepG2 cell nuclei in the 3D space of the parameters are shown, respectively. In Fig. 4c, both are shown again together, each with the additional mean data point, in the same respective color—namely green for HeLa and red for HepG2—in a darker shade to be recognized. For the mean points, the projections to the three embedding planes of the parameters in the space have also been traced, to allow for better identification of the 3D position. Additional alternative representations of these data in the 3D space are shown in Fig.S4, which allows to visualize the overall positions of the respective populations as ellipsoidal clusters. Finally, in Fig. 4d, the same mean values of 3D coordinates are plotted for each cell type, with error bars representing ± 1 standard deviation. For all three parameters, statistically significant differences appeared between the populations of the two cell types. The difference between the mean values of FD seems to be very low; nevertheless, the error bars are also much smaller for this parameter than for the other two—probably due to a more robust measurement procedure or intrinsically characteristic nature of the FD quantity itself. As a result, the means are statistically different, with very high significance level (***). The same marked statistical difference appears for TPD (***). Finally, for R_{max}, where apparently some overlap of the respective distributions emerges, the means are still significantly different, even if with a lower significance level (**).

One critical point was to evaluate if the observed differences were simply due to the random occurrence of other factors not associated with the intrinsic differences between the nuclei populations. Therefore, as a first step, the experiment was repeated, which provided the dataset called run#2. These results are shown in Fig.S5 and basically confirm the differences between the two populations of cells. Not only were the pairs of values for each parameter in Fig.S5 different, as previously observed in Fig. 4, but—above all—the observed differences pointed to the same direction. Actually,

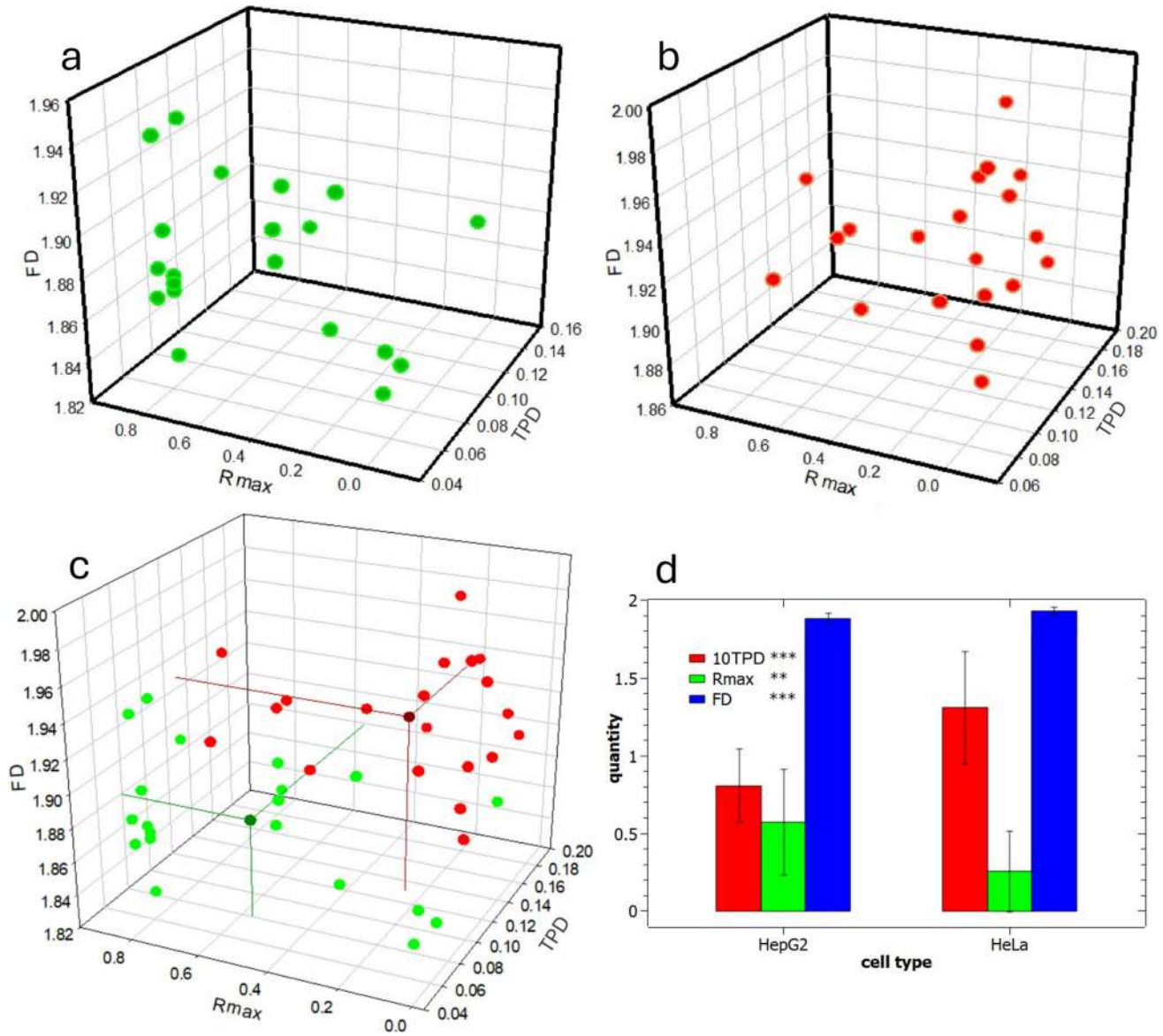

Fig. 4 Experimental data for comparison of HeLa and HepG2 cell nuclei chromatin patterns during run#1 experiment. **a** Data points for HeLa cells, **b** data points for HepG2 cells, **c** combined data of (**a**) and (**b**) with the respective mean points, **d** plot of means ± standard deviation for each of the three parameters for the two cell types (TPD in shown red, R_{max} in green, and FD in blue); results of ANOVA showed significant difference in all cases

also in run#2, HeLa nuclei showed higher TPD (***), lower R_{max} (*), and higher FD (***) than HepG2 nuclei, with only a minor decrease in overall difference scores (with a total score of seven "star" units instead of eight).

Discussion

One technical limitation during our measurements was that the Hoechst fluorophore is usually excited—by single photons—in the UV range of the light spectrum and undergoes consequent emission in the blue region. However, our confocal microscope has no UV excitation source; instead, it has a supercontinuum white light laser in the 440–800 nm range. Initially, we also tried to excite Hoechst in the long wavelength foot of its absorption spectrum at 440 nm, but the signal was of too low quality (SNR ≈1). Therefore, we used the other laser available in the system for stimulated emission depletion, working at 775 nm wavelength, in two-photon excitation mode (2PE) (Diaspro et al. 2007). This way, two photons impinging simultaneously on the sample (on the timescale of the order of 1 fs) can contribute each roughly half the energy—and thus have twice the wavelength—than the single-photon excitation case. Of course,

much higher peak laser power is required for 2PE (we used it at 100% power, corresponding to ≈400 mW at the focal plane), which obviously is still not too invasive, thanks to the point of the laser being pulsed (at 80 MHz). Therefore, our source used in 2PE mode was equivalent to single-photon excitation with a wavelength of ≈388 nm, well within the Hoechst absorption spectrum. Whereas using a doughnut-shaped beam is expected to somewhat diminish the confocal resolution expected after the theoretical diffraction limit, it has been shown in (Bianchini and Diaspro 2012) that in practice only a minor effect is observed in this direction, when a good signal-to-noise ratio is obtained.

Since our confocal images were diffraction-limited to ≈250 nm resolution, according to the Nyquist–Shannon sampling rule we selected a pixel size ≈100 nm. This relatively large pixel size, associated with an image size of 1024 × 1024 pixels, i.e.,102.4 × 102.4 μm^2, allowed us to image several nuclei within a single image scan. Thus, we had quite some redundancy in the number of nuclei to select for analysis in our experiment. We decided to select the nuclei that showed best contrast and were neither affected by protruding bumps or intruding cavities, nor too much elongated or deviating significantly from oval shape (see Fig.S3). The last requirement was due to the point of having to approximate the nuclear envelope with an ellipse, see"Image analysis". As mentioned in the Experimental section, we found it convenient to acquire images with a field of view sufficiently large to collect several nuclei per image instead of a single one. This is because the typical size of a single nucleus is relatively small (maximum around 10 μm diameter), and at the set digital resolution (around 100 nm per pixel), scanning single-nucleus images would require little more than 100 × 100 pixels, which would have definitely been unnecessarily small. This allowed us to work pretty fast in the imaging step. Most of the work done in this experiment actually focused on defining the protocols for calculating the parameters, applying them to our images, and analyzing the statistical significance of our results.

The importance of FD in describing chromatin structure has already been pointed out extensively in the literature (Almassalha et al. 2017; Boettiger et al. 2016; Metze et al. 2019; Mirny 2011; Yi et al. 2015). There exist several other methods for carrying out the fractal analysis of images in Fiji, according to different plugins (e.g., Fraclac (Karperien 2012), which can also calculate lacunarity (da Fonseca de Albuquerque et al. 2022; Ţălu et al. 2020)). However, we decided to keep extraction of this traditional image parameter as simple and straightforward as possible, using the default FD calculation method of Fiji. Binarization for subsequent extraction of FD is a somewhat arbitrary step in that the result depends critically on the position set for the threshold on the signal intensity of DNA inside the nucleus. We initially tried several automated criteria available in Fiji for this binarization operation (the better ones apparently being, in our case, Moments or Otsu). However, we did not find consistent results throughout all the nuclei images when doing so. Therefore, we preferred to set the threshold manually. Since we did not subtract the background offset and set the threshold considering all the pixels in the cropped nucleus image (rectangular area including background), the narrow population of lowest background counts appeared in the distribution of intensity levels, which was clearly distinguishable from the population of bright pixels corresponding to labeled nucleus regions, recognizable as a much broader symmetric band centered around higher intensity levels. In all cases, we set our threshold to the peak position of this band (corresponding also to the median value).

The parameter called here TPD has already been used in Irianto et al. ((Irianto et al. 2014)), where it was used to describe the change in chromatin pattern of chondrocytes on altering their osmotic pressure. They called this quantity with the different name of CCP, namely chromatin condensation parameter. We preferred not to adopt the same name, as we think that this parameter, while useful, is not by itself alone a full descriptor of the chromatin condensation. Actually, the two parameters of CCP and FD together describe to deeper extent the chromatin compaction, in terms of intensity and characteristic sub-structure spacing, respectively.

The third parameter R_{max} was selected to identify the characteristic distance from the nucleus center at which the maximum chromatin compaction, described by FD and TCP, would eventually occur. One possible criticism about R_{max} points to the nonlinear change applied to the nuclei center-to-edge distances during circularization. However, the advantage of making it possible to compare all radial distances and—after normalization to 1—for nuclei of all size, makes this parameter interesting. In perspective, R_{max} could eventually be associated with the amount of balance between euchromatin, which is assumed to stay closer to the nuclear lamina, and heterochromatin, which is supposed to remain closer to the inner regions of the nuclei. However, for the moment this is just bare speculation, as we have already pointed out that insight in functional interpretation of the observed differences is beyond the scope of the present work. So, we limit our comments to the performance of our three parameters in describing the differences between the two populations of test cell nuclei studied here.

In calculating $R_{max,}$ we made a selection of nuclei of elliptical shape only, discarding the irregularly shaped ones (for details see Experimental section and Fig.S3). The discarded nuclei were actually a small part of the total, around 30%, for both cell types. Additionally, whereas we are aware that nuclei can have irregular morphology due to a number of factors, both physiological and pathological, as well as an effect of sample preparation, there are no reasons to doubt that also the subset of regular (i.e., elliptical)-shaped

nuclei is anyway representative of the whole population of the respective cell type.

The significance of the differences between the means of all R_{max} between HepG2 and HeLa cell nuclei was assessed with the ANOVA test shown in Figs.4d and Fig. 5 (and confirmed with the same in Fig.S5d). However, we can also wonder if the means of all radial profiles for a single nuclei population can give similar insight, and how the positions of the maximum for the mean profile compares with the mean positions of the maxima for each individual profile. Therefore, we carried out a similar analysis for the dataset of experiment run#1, the same represented in Fig. 4, and the results are shown in Fig.S6 (details see Supplementary Information). Obviously, the position of the maximum of the mean plots does not coincide with the mean of the positions of each maximum, as the process of extracting a maximum is nonlinear. Nevertheless, qualitatively the information obtained is similar: we see from Fig.S6 that the HepG2 nuclei exhibit a maximum of the mean profile shifted quite close to the outer edge, at ~0.85, whereas for the HeLa nuclei this maximum occurs at ~0.13. These positions are clearly more spaced apart from each other than those resulting from the means (0.57 and 0.25, respectively), yet they rank in the same order. In Fig. S6, the bands around the mean profile in both cases show the observed uncertainty: in red, the band associated with ±1 standard deviation width is shown, whereas in green is the band with ±1 standard error. In both cases, despite the relatively large uncertainty, the different behavior is

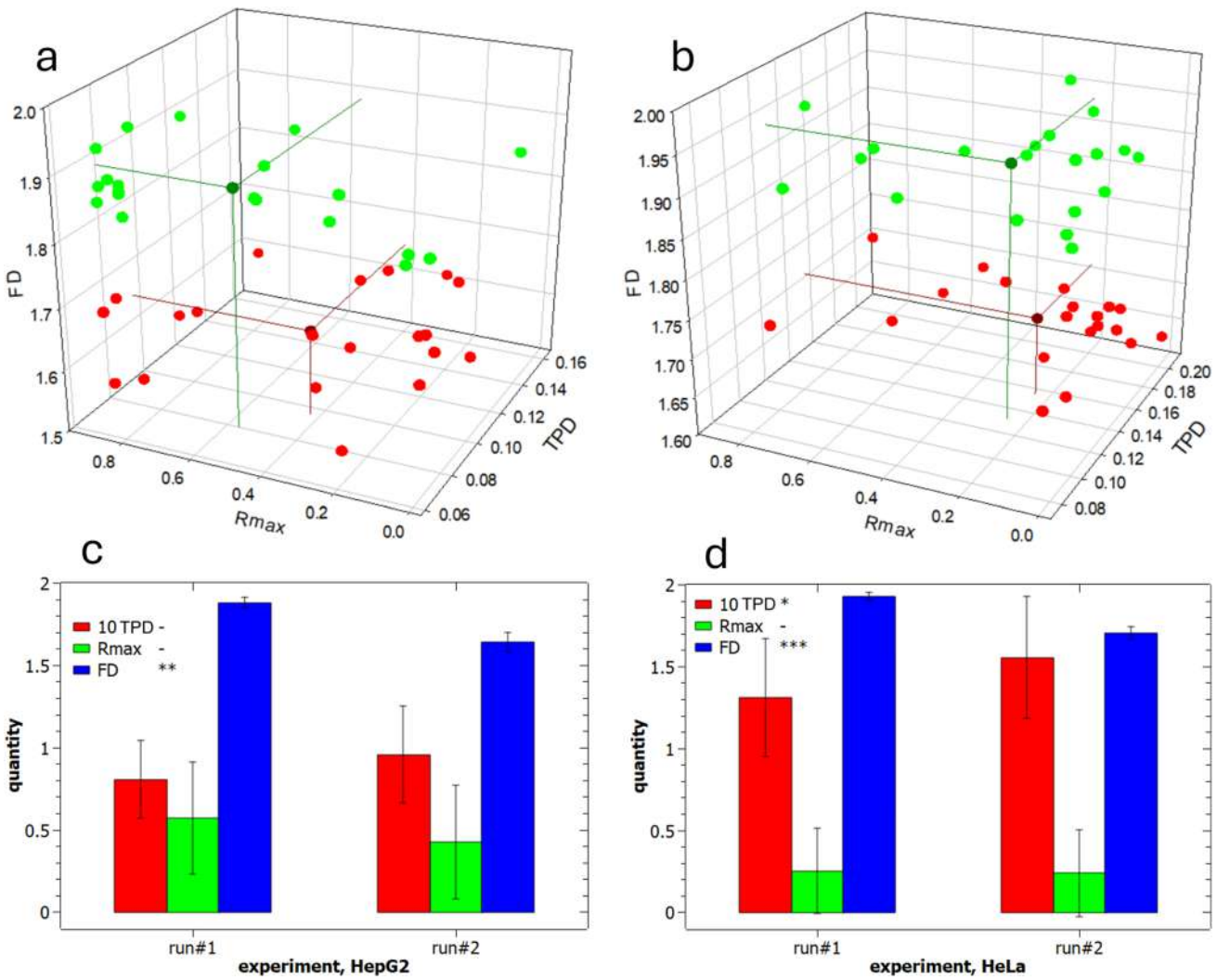

Fig. 5 Experimental data for comparison of run#1 and #2 datasets. **a** Run#1 and run#2 data points for HepG2 cell nuclei, **b** run#1 and run#2 data points for HeLa cell nuclei. **c** and **d** present the respective plots (for HepG2 and HeLa nuclei) of means ± standard deviation for each of the three parameters for the two runs of the experiment (TPD in shown red, R_{max} in green, and FD in blue); results of ANOVA showed significant differences in several cases (for details see main text)

clear and confirms and strengthens the difference observed based on the population of single R_{max} values.

Overall, Fig. 4 (run#1) and Fig.S5 (run#2) show significant differences between the cell types considered. However, despite the results being confirmed during the second, repeated experiment, these could still be due to a lucky and unlikely occurrence of, e.g., systematic errors and possess no real physical meaning. Therefore, the final cross-check requested to validate our observations would be that the two datasets, run#1 and run#2, do not show statistically significant differences—at least not to the same degree—between the old (run#1) and new (run#2) set of data for the same cell type. To test this null hypothesis, we carried out a similar comparison as that between the cell types, and the results are presented in Fig. 5. Actually, from the panels in Fig. 5c, d one can see that the ANOVA pointed out some statistically significant differences also in these two comparisons. In particular, FD differed between run#1 and #2, both for the HepG2 (**) and—even more—for the HeLa nuclei (***). However, for the other two parameters, only in one case out of four a significant difference appeared, for the TPD values of HeLa nuclei, which was at the lowest significance level (*). HeLa cells appear to be more variable across their own total population (a total of four "stars" difference for all parameters vs the two "stars" of HepG2). In particular, FD is the most sensitive parameter (2 "stars" on average): it may be the case that the evaluated uncertainty for this figure is somewhat underestimated. We conclude that its apparent robustness is more from the point of view of mathematical calculation rather than in the physical contents. Nevertheless, overall, a total—average—score of 3 "stars" emerged (2 for HepG2 and 4 for HeLa), as compared to the average score in the difference of 7.5 "stars" between cell types (8 for run#1 and 7 for run#2). Therefore, this much lower extent of observed differences at least partly confirms our hypothesis in support of using the selected parameters. The minor differences between different sampling datasets for the same cell type may be due to a relevant intrinsic variability of each cell population, following the point that the cells are not synchronized in a given phase of their life cycle, as well as to the limited statistics, an effect that could be mitigated in the future by taking a larger number of images for each case, e.g., $N = 40$ or 60.

Another limitation of our work is in the actual biological scope. In fact, the selection of the cell lines did not correspond to any particular biological question, nor did we intend to draw any conclusions about the compared cell lines. We are aware that, for example, even the prolonged passaging of cell cultures may affect nuclear morphology and chromatin compaction, and this effect should be taken into account when comparing cells with a precise biological goal. However, the present types of cells have been selected only as representative of different cell populations, as test samples to see if any difference may be found by our set of describing parameters, and how strong this discrimination can be.

In view of possible future refinement of the image analysis protocol presented in this work, averaging the radial profiles of nucleus intensity (here aimed at obtaining the R_{max} values) appears to be the procedure with the most potential for additional insight. As shown previously, the results occurring after averaging R_{max} values in a population can be cross-checked by looking at the single R_{max} from the mean profile obtained after averaging them altogether (as in Fig.S6). Additionally, the absolute maximum is probably just a piece of information hidden in the respective profile. Complementary data could be the prominence of such a maximum—how much above the mean intensity—and the possible occurrence of a minimum (other than the zero close to normalized radial distance $x = 1$) or the presence of a secondary maximum in a different position.

Conclusion

In this work, three parameters were defined to describe the different patterns in chromatin distribution inside cell nuclei. These parameters were tested on fixed cell samples of cell types available at our laboratory, representing two types of cancer cells, as test samples. Altogether, the identified 3D space of parameters appeared to allow successful distinction of the cell types. Some variations between different subsets of the same type of cells also appeared. This is probably due to the dependency on the cell life cycle, which adds to the different types of tissue cells. Nevertheless, we have here laid the foundations for a methodological approach to cell nuclei image analysis, which could be used in the future for more comprehensive studies, including improved control of cell samples, for example, including controls of healthy cells with the same type of tissue as the sick ones (e.g., healthy cervix and liver cells, to be compared with our HeLa and HepG2 cells). Even more interestingly, having the capability to fix cells at different times during their life cycle will likely make it possible not only to have more narrow distributions of the three characteristic parameters, but also to define characteristic values thereof for each phase of the cell life, more readily associated with the presence of hetero- and euchromatin. The present method, applied here on diffraction-limited resolution images of confocal microscopy, would also be viable with images obtained with more advanced imaging techniques such as STED or MINFLUX and benefit of the respective super-resolution.

Supplementary Information The online version contains supplementary material available at https://doi.org/10.1007/s00249-025-01770-y.

Acknowledgements This work was carried out in the frame of the project SEELIFE ("StrEngthEning the ItaLIan InFrastructure of Euro-bioimaging"), which was funded by the European Union—Next Generation EU PNRR MUR Infrastructure program (B53C22001810006, IR0000023)

Authors' contributions VB and EG prepared the samples; MR did the imaging; MS did the image processing and analysis, carried out the statistical analysis, and drafted the manuscript; AD supervised and directed the work; all authors revised the manuscript.

Funding Directorate-General for Research and Innovation,Next Generation EU PNRR MUR Infrastructure program (B53C22001810006,Alberto Diaspro,IR0000023),Alberto Diaspro

Data availability The data that support the findings of this study are available from the corresponding author, upon request.

Declarations

Conflict of interest The authors declare no competing interests.

References

Abràmoff MD, Magalhaes PJ, Ram SJ (2004) Image processing with imageJ. Biophoton Int. 11(7):36–42

Almassalha LM, Tiwari A, Ruhoff PT, Stypula-Cyrus Y, Cherkezyan L, Matsuda H, Dela Cruz MA, Chandler JE, White C, Maneval C, Subramanian H, Szleifer I, Roy HK, Backman V (2017) The global relationship between chromatin physical topology, fractal structure, and gene expression. Sci Rep. https://doi.org/10.1038/srep41061

Baggethun P. (2002) *Radial profile Fiji plugin*. https://imagej.net/ij/plugins/radial-profile.html

Benke A, Manley S (2012) Live-cell dSTORM of cellular DNA based on direct DNA labeling. ChemBioChem 13(2):298–301. https://doi.org/10.1002/cbic.201100679

Bianchini P, Diaspro A (2012) Fast scanning STED and two-photon fluorescence excitation microscopy with continuous wave beam. J Microsc 245(3):225–228. https://doi.org/10.1111/j.1365-2818.2011.03577.x

Boettiger AN, Bintu B, Moffitt JR, Wang S, Beliveau BJ, Fudenberg G, Imakaev M, Mirny LA, Wu CT, Zhuang X (2016) Super-resolution imaging reveals distinct chromatin folding for different epigenetic states. Nature 529(7586):418–422. https://doi.org/10.1038/nature16496

Burgers TCQ, Vlijm R (2023) Fluorescence-based super-resolution-microscopy strategies for chromatin studies. Chromosoma 132(3):191–209. https://doi.org/10.1007/s00412-023-00792-9

da Fonseca de Albuquerque MD, Bastos DC, Ţălu Ş, Matos RS, Pires MA, Salerno M, Da Fonseca Filho HD, Simão RA (2022) Vapor barrier properties of cold plasma treated corn starch films. Coatings. https://doi.org/10.3390/coatings12071006

Diaspro A, van Zandvoort MAMJ (2021) Super-resolution imaging in biomedicine. CRC, Boca Raton

Diaspro A, Schneider M, Bianchini P, Caorsi V, Mazza D, Pesce M, Testa I, Vicidomini G, Usai C, Van den Bos A (2007) Two-photon excitation fluorescence microscopy. Sci Microscopy. https://doi.org/10.1007/978-0-387-49762-4_11

Durie BGM, Vaught L, Chen YP, Olson GB, Salmon SE, Bartels PH (1978) Discrimination between human T and B lymphocytes and monocytes by computer analysis of digitized data from scanning microphotometry. I. Chromatin distribution patterns. Blood 51(4):579–589. https://doi.org/10.1182/blood.V51.4.579.579

García-Cabezas M, Barbas H, Zikopoulos B (2018) Parallel development of chromatin patterns, neuron morphology and connections: potential for disruption in autism. Front Neuroanat. https://doi.org/10.3389/fnana.2018.00070

Hansen JC (2012) Human mitotic chromosome structure: what happened to the 30-nm fibre? EMBO J 31(7):1621–1623. https://doi.org/10.1038/emboj.2012.66

Irianto J, Lee DA, Knight MM (2014) Quantification of chromatin condensation level by image processing. Med Eng Phys 36(3):412–417. https://doi.org/10.1016/j.medengphy.2013.09.006

Kak, S. (2023). *The geometry of chromatin*. https://doi.org/10.36227/techrxiv.23818902.v1

Karperien, A. (2012). *FracLac Fiji plugin*. https://imagej.net/ij/plugins/fraclac/FLHelp/Introduction.htm

Kostiuk G, Bucevičius J, Gerasimaitė R, Lukinavičius G (2019) Application of STED imaging for chromatin studies. J Phys D. https://doi.org/10.1088/1361-6463/ab4410

Lakadamyali M, Cosma MP (2015) Advanced microscopy methods for visualizing chromatin structure. FEBS Lett 589(20):3023–3030. https://doi.org/10.1016/j.febslet.2015.04.012

Maraldi NM, Lattanzi G, Squarzoni S, Sabatelli P, Marmiroli S, Ognibene A, Manzoli FA (2003) At the nucleus of the problem: nuclear proteins and disease. Adv Enzyme Regul 43:411–443. https://doi.org/10.1016/S0065-2571(02)00042-0

Mascetti G, Vergani L, Diaspro A, Carrara S, Radicchi G, Nicolini C (1996) Effect of fixatives on calf thymocytes chromatin as analyzed by 3D high-resolution fluorescence microscopy. Cytometry 23(2):110–119. https://doi.org/10.1002/(SICI)1097-0320(19960201)23:2%3c110::AID-CYTO4%3e3.0.CO;2-O

The MathWorks Inc. (2023) MATLAB version: R2023b, Natick, Massachusetts: The MathWorks Inc. https://www.mathworks.com

Metze K, Adam R, Florindo JB (2019) The fractal dimension of chromatin - a potential molecular marker for carcinogenesis tumor progression and prognosis. Exp Rev Mol Diagnostics 19(4):299–312. https://doi.org/10.1080/14737159.2019.1597707

Mirny LA (2011) The fractal globule as a model of chromatin architecture in the cell. Chromosome Res 19(1):37–51. https://doi.org/10.1007/s10577-010-9177-0

Mishra LN, Thiriet C, Vasudevan D (2023) Editorial: chromatin structure and function. Front Gene. https://doi.org/10.3389/fgene.2023.1140534

Nishino Y, Eltsov M, Joti Y, Ito K, Takata H, Takahashi Y, Hihara S, Frangakis AS, Imamoto N, Ishikawa T, Maeshima K (2012) Human mitotic chromosomes consist predominantly of irregularly folded nucleosome fibres without a 30-nm chromatin structure. EMBO J 31(7):1644–1653. https://doi.org/10.1038/emboj.2012.35

Pierzynska-Mach A, Cainero I, Oneto M, Ferrando-May E, Lanzanò L, Diaspro A (2023a) Imaging-based study demonstrates how the DEK nanoscale distribution differentially correlates with

epigenetic marks in a breast cancer model. Sci Rep. https://doi.org/10.1038/s41598-023-38685-7

Pierzynska-Mach A, Czada C, Vogel C, Gwosch E, Osswald X, Bartoschek D, Diaspro A, Kappes F, Ferrando-May E (2023b) DEK oncoprotein participates in heterochromatin replication via SUMO-dependent nuclear bodies. J Cell Sci. https://doi.org/10.1242/jcs.261329

Russ JC (1994) Fractal Surfaces. Springer

Russ JC (2011) The image processing handbook, 6th edn. CRC Press, Boca Raton

Sahota TS, Peet FG, Ibaraki A, Farris SH (1986) Chromatin distribution pattern and cell functioning. Can J Zool 64(9):1908–1913. https://doi.org/10.1139/z86-286

SciDAVis plotting software. (n.d.). Retrieved January 29, 2025, from https://scidavis.sourceforge.net

SigmaPlot web page. (n.d.). Retrieved January 29, 2025, from https://www.sigmaplot.com

Takizawa Y, Kurumizaka H (2022) Chromatin structure meets cryo-EM: dynamic building blocks of the functional architecture. Biochimica Et Biophysica Acta Gene Regul Mech. https://doi.org/10.1016/j.bbagrm.2022.194851

Ţălu Ş, Abdolghaderi S, Pinto EP, Matos RS, Salerno M (2020) Advanced fractal analysis of nanoscale topography of Ag/DLC composite synthesized by RF-PECVD. Surf Eng 36(7):713–719. https://doi.org/10.1080/02670844.2019.1710937

Van Steensel B (2011) Chromatin: constructing the big picture. EMBO J 30(10):1885–1895. https://doi.org/10.1038/emboj.2011.135

Yi J, Stypula-Cyrus Y, Blaha CS, Roy HK, Backman V (2015) Fractal characterization of chromatin Decompaction in live cells. Biophys J 109(11):2218–2226. https://doi.org/10.1016/j.bpj.2015.10.014